

# CIP/multi-moment finite volume method for Euler equations: A semi-Lagrangian characteristic formulation

S. Ii, F. Xiao \*

*Department of Energy Sciences, Tokyo Institute of Technology, 4259 Nagatsuta, Midori-ku, Yokohama 226-8502, Japan*

Received 3 April 2006; received in revised form 27 July 2006; accepted 21 August 2006

Available online 10 October 2006

---

## Abstract

An accurate algorithm for the hyperbolic equations has been proposed by combining the *constrained interpolation profile/multi-moment finite volume method* (CIP/MM FVM) with the characteristic theory. Two types of moments, i.e. the point value (PV) at cell boundary of each mesh element and the volume-integrated average (VIA) over each mesh cell of a physical field, are treated as the model variables and updated independently in time. The interpolation that uses both PV and VIA is reconstructed for each Riemann invariant of the hyperbolic conservation laws. The PVs are then updated by semi-Lagrangian schemes along the characteristic curves, while the VIAs are computed by formulations of flux form, where the numerical fluxes are evaluated by averaging the physical fields over the characteristic curves. The Runge–Kutta type schemes are used for integrating the trajectory equations based on the characteristic speeds to improve the accuracy in time.

The numerical procedure for the one-dimensional Euler conservation laws is described in detail in this paper. Number of benchmark tests are presented. The numerical results show that the present method is accurate and competitive to other existing methods.

© 2006 Elsevier Inc. All rights reserved.

*Keywords:* Finite volume method; Hyperbolic equation; CIP; Multi-moment; Characteristics; Semi-Lagrangian scheme; Compressible flow

---

## 1. Introduction

Many high resolution finite volume schemes have been so far developed for the Euler conservation laws that have direct applications in aerodynamic engineering. A finite volume method (FVM) is cast in a flux form and thus guarantees the numerical conservation which is found to be essential to capturing shock waves with correct position. In a conventional finite volume method, the discretized model variable of physical field is usually defined as the volume-integrated average (VIA), or cell-integrated average, over the control volume. The

---

\* Corresponding author. Tel./fax: +81 45 924 5538.

E-mail address: [xiao@es.titech.ac.jp](mailto:xiao@es.titech.ac.jp) (F. Xiao).

numerical flux on each control volume boundary is approximated by an interpolation reconstruction based on the VIA for each physical field. A high resolution scheme requires the reconstruction to be built in such a way so that the numerical solution has an accuracy higher than second-order for the smooth region, but does not produce significant numerical oscillations in the presence of the discontinuities. Representative schemes of this category are the monotone upwind scheme for conservation laws (MUSCL) [21], the total variation diminishing (TVD) [6], the piecewise parabolic method (PPM) [1], the piecewise rational method (PRM) [35], the essentially non-oscillatory (ENO) [7,17,18], and the weighted ENO (WENO) [11,9]. In these methods, only the VIA is used as the model variable which is stored and predicted in time. Thus, a high order reconstruction needs a wide stencil of computation grid, which makes the extension of such a method to unstructured grid not a easy task.

Different from the above-mentioned conventional conservative high resolution schemes, where only the VIA of each physical field is treated as the model variable to be put forward in time, the discontinuous Galerkin (DG) method [2–5] makes use of some extra moments in addition to the VIA-equivalent quantity as the model variables too. The VIA-equivalent moment in a DG method is effectively updated through a finite volume formulation of flux form, and therefore is numerically conserved. A high-order reconstruction can be built with high-order basis functions in a DG method by increasing the local degrees of freedom (DOF) within each control volume (mesh element). Each moment (or DOF) in a DG method has its own evolutionary governing equation derived from the Galerkin formulation, which involves numerical quadratures. Another way to increase local DOF is found in the spectral finite volume (SV) method [23–26], where each mesh cell or spectral volume (SV) is subdivided into smaller regions, namely control volumes (CVs). The VIA of physical field is then defined over each CV and updated separately in time. So, high-order polynomials can be piecewisely constructed over each SV, and the Riemann problems among the CV of the same SV can be solved exactly. A recent study [23], however, showed that more restrictive CFL condition for computational stability is required for higher order approximations of either DG or SV method.

An alternative to increase the local DOF is found in the constrained interpolation profile (CIP) method [36,38], where more than two types of moments, i.e. the point value (PV) and the first-order derivatives (DV) are simultaneously treated as the model variables and predicted independently in time. Successive studies have resulted in a class of conservative schemes [20,37,28,29], so called CIP-conservative semi-Lagrangian (CIP-CSL) methods, for the scalar conservative advection transport. In a CIP-CSL scheme, a moment of VIA is introduced as a new model variable that is updated by a flux-form formulation and exactly conserved. More recently, a more general finite volume framework, the CIP/multi-moment finite volume method (CIP/MM FVM), has been proposed and implemented to various fluid dynamic simulations [30–34]. Using multi-moment, a CIP/MM FVM can construct the high-order interpolation function on a local base, which makes the implementation of the method on unstructured mesh much easier. We, for example, have devised a fourth-order and single-cell based advection scheme on triangular unstructured mesh [8].

A similar multi-moment concept has been used in the Hermite WENO (HWENO) scheme [12] that makes the stencil much more compact than the conventional WENO scheme. In general, making use of multi-moments enables one to reconstruct high-order interpolation function with local stencil.

In the CIP/MM FVM, the way to update the moment is more ‘physically motivated’ and more flexible. In regard to the hyperbolic conservation systems, for example, we compute the VIA (conservative moment) through a flux-form formulation to achieve the numerical conservativeness, and update the PV (non-conservative moment) by a semi-Lagrangian procedure. As shown in [8], a CIP/MM FVM works well even with a larger CFL number. Concerning the computation of the Euler equations, a CIP/MM FVM has been developed by using a pressure projection [32,33]. The resulting algorithm conserves numerically the VIA of the conservative variables in the Euler equations, and works for all Mach numbers.

In this paper, we present another more accurate variant of the CIP/MM FVM to the one-dimensional inviscid Euler conservation laws by fully implementing the characteristic theory to the system. The semi-Lagrangian solutions are solved in terms of the Riemann invariants along the characteristic curves, and used also to evaluate the numerical fluxes for updating the VIAs of the conservative variables. It results in a robust and accurate formulation for the Euler conservation laws.

In Section 2, we describe the CIP/MM FVM for the scalar conservation law, where the definition for the moments, the CIP-CSL reconstructions and the way to update the moments are given in detail. The imple-

mentation of the CIP/MM FVM to the one-dimensional Euler conservation laws is discussed in Section 3, and the numerical experiments for the Euler conservation laws are shown in Section 4. We evaluated our method with some typical benchmark tests. Finally, some discussions and conclusion remarks end the paper in Section 5.

## 2. The scalar conservation laws

In this section, we describe the numerical formulation of the CIP/MM FVM for the scalar conservative advection transport equation as follows:

$$\frac{\partial \phi}{\partial t} + \frac{\partial(u\phi)}{\partial x} = 0, \tag{1}$$

where  $\phi$  is the transported field quantity and  $u$  is the velocity.

### 2.1. Moments definition

We solve (1) on one-dimensional domain divided into control volumes (mesh cells)  $[x_{i-1/2}, x_{i+1/2}]$ ; ( $i = 1, 2, \dots, I$ ). Shown in Fig. 1, two kinds of moments are defined respectively for the field variable  $\phi(x, t)$  as

- the volume-integrated average (VIA) over each mesh cell

$$\overline{V}\phi_i = \frac{1}{\Delta x_i} \int_{x_{i-1/2}}^{x_{i+1/2}} \phi(x, t) dx, \tag{2}$$

where  $\Delta x_i = x_{i+1/2} - x_{i-1/2}$ , and

- the point value (PV) at cell boundary

$$\overline{P}\phi_{i+1/2} = \phi\left(x_{i+1/2}, t\right). \tag{3}$$

Several conservative CIP schemes [20,37,28,29], i.e. the CIP-CSL schemes, have been proposed to solve the advection transport equation (1). In a CIP-CSL scheme, the VIA and PV of  $\phi(x, t)$  are simultaneously treated as the model variables, and the interpolation functions are built up by using both VIA and PV. We show two practical CIP-CSL reconstructions below.

### 2.2. The interpolation functions

#### 2.2.1. CIP-CSL2 reconstruction [37]

Given one VIA  $\overline{V}\phi_i$  and two PVs  $\overline{P}\phi_{i\pm 1/2}$  over  $[x_{i-1/2}, x_{i+1/2}]$ , we construct a piecewise quadratic interpolation function for cell  $i$ ,

$$\Phi_i(x) = a_2\left(x - x_{i-1/2}\right)^2 + a_1\left(x - x_{i-1/2}\right) + a_0. \tag{4}$$

From the constrained conditions

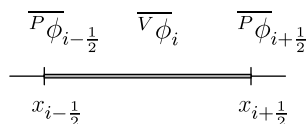


Fig. 1. The locations of the moments for the one-dimensional scalar equation on cell  $i$ .

$$\begin{aligned}
\Phi_i(x_{i-\frac{1}{2}}) &= \overline{P\phi}_{i-\frac{1}{2}}, \\
\Phi_i(x_{i+\frac{1}{2}}) &= \overline{P\phi}_{i+\frac{1}{2}}, \\
\frac{1}{\Delta x_i} \int_{x_{i-\frac{1}{2}}}^{x_{i+\frac{1}{2}}} \Phi(x) dx &= \overline{V\phi}_i,
\end{aligned} \tag{5}$$

we have the coefficients of (4) as

$$\begin{aligned}
a_0 &= \overline{P\phi}_{i-\frac{1}{2}}, \\
a_1 &= \frac{2(3\overline{V\phi}_i - \overline{P\phi}_{i+\frac{1}{2}} - 2\overline{P\phi}_{i-\frac{1}{2}})}{\Delta x_i}, \\
a_2 &= \frac{3(-2\overline{V\phi}_i + \overline{P\phi}_{i+\frac{1}{2}} + \overline{P\phi}_{i-\frac{1}{2}})}{\Delta x_i^2}.
\end{aligned} \tag{6}$$

### 2.2.2. CIP-CSL3 reconstruction [28]

In addition to (5), we include another parameter, the first-order derivative  $d_i$  at the cell center, and use the following constrained conditions

$$\begin{aligned}
\Phi_i(x_{i-\frac{1}{2}}) &= \overline{P\phi}_{i-\frac{1}{2}}, \\
\Phi_i(x_{i+\frac{1}{2}}) &= \overline{P\phi}_{i+\frac{1}{2}}, \\
\frac{1}{\Delta x_i} \int_{x_{i-\frac{1}{2}}}^{x_{i+\frac{1}{2}}} \Phi(x) dx &= \overline{V\phi}_i, \\
\left. \frac{d\Phi}{dx} \right|_{x=x_i} &= d_i.
\end{aligned} \tag{7}$$

A piecewise cubic interpolation function is constructed over cell  $i$  as follows:

$$\Phi_i(x) = a_3 \left(x - x_{i-\frac{1}{2}}\right)^3 + a_2 \left(x - x_{i-\frac{1}{2}}\right)^2 + a_1 \left(x - x_{i-\frac{1}{2}}\right) + a_0,$$

with

$$\begin{aligned}
a_0 &= \overline{P\phi}_{i-\frac{1}{2}}, \\
a_1 &= \frac{2(3\overline{V\phi}_i - 3\overline{P\phi}_{i-\frac{1}{2}} - \Delta x_i d_i)}{\Delta x_i}, \\
a_2 &= \frac{3(-2\overline{V\phi}_i - \overline{P\phi}_{i+\frac{1}{2}} + 3\overline{P\phi}_{i-\frac{1}{2}} + 2\Delta x_i d_i)}{\Delta x_i^2}, \\
a_3 &= \frac{4(\overline{P\phi}_{i+\frac{1}{2}} - \overline{P\phi}_{i-\frac{1}{2}} - \Delta x_i d_i)}{\Delta x_i^3}.
\end{aligned} \tag{8}$$

The first-order derivative or gradient of the interpolation function  $d_i$  can be computed in terms of the known moments, i.e. the PV and VIA. Shown later, the gradient  $d_i$  provides a possibility for us to modify the interpolation function, thus to make the numerical solution to possess some properties desired. For example, numerical oscillation can be effectively eliminated by simply implementing some existing slope limiters (see [28] for details). We should also notify [14] for another way of reconstruction with a Hermite interpolation.

We give two approximations for  $d_i$  below.

• Second-order approximation

The second-order approximation for  $d_i$  is obtained by using cell boundary PVs  $\overline{P\phi}_{i\pm 1/2}$  of cell  $i$ ,

$$d_i = \frac{\overline{P\phi}_{i+\frac{1}{2}} - \overline{P\phi}_{i-\frac{1}{2}}}{\Delta x}. \tag{9}$$

It is obvious that with the coefficient of the third-order term vanishing in (8), the cubic interpolation function becomes a quadratic one. Thus, the CIP-CSL3 reconstruction degrades to the CIP-CSL2 reconstruction. So, the CSL2 reconstruction can be effectively expressed as a special case of (8). Moreover, as shown later, recasting the CSL2 reconstruction into (8) with the slope evaluated by (9), we are able to introduce a limiting projection to suppress the numerical oscillations in the original CIP-CSL2 scheme.

• Fourth-order approximation

The fourth-order approximation for  $d_i$  is obtained by using the VIAs  $\overline{V\phi}_{i\pm 1}$  and the boundary PVs  $\overline{P\phi}_{i\pm 1/2}$  of two neighboring cells,

$$d_i = \frac{-\overline{V\phi}_{i+1} + 10\overline{P\phi}_{i+\frac{1}{2}} - 10\overline{P\phi}_{i-\frac{1}{2}} + \overline{V\phi}_{i-1}}{8\Delta x}, \tag{10}$$

for uniform grid. Compared to the formula in [28], the stencil of the fourth-order approximation (10) is more compact.

In this paper, we use the cubic polynomial (8) as the unified form of the interpolation function. The resulting reconstruction function is either a quadratic or a cubic polynomial with the slope parameter  $d_i$  approximated either by (9) or by (10).

As discussed in our previous papers, the introduction of the slope parameter  $d_i$  provides us a convenient way to control both the numerical oscillation and diffusion. Next, we discuss a numerical switching using the TVB concept to control  $d_i$  and the numerical oscillations hence.

2.2.3. Slope limiting

High-order reconstructions tend to cause Gibbs phenomena near a discontinuity. Some solution-dependent switchings have to be devised to suppress the numerical oscillations in the presence of the discontinuity or large jump. It is well known that the TVD [6] type schemes degrade to first-order not only at a discontinuity but also at an extremum in the solution. Thus, less restrictive limitings must be considered if one desires higher order schemes. For example, the total variation bounded (TVB) [15] concept works well with some recent high-order schemes such as the DG and the SV methods. The TVB scheme maintains high-order accuracy even at extrema, hence is able to give a globally high-order accuracy.

We adopt the TVB limiting to gradient  $d_i$  which is at first approximated by (9) or (10). The modified TVB-minmod limiter [15] is written as

$$d_i^* = \begin{cases} d_i & \text{if } |d_i| \leq M\Delta x, \\ \text{minmod}(d_i, d_{i-\frac{1}{2}}, d_{i+\frac{1}{2}}) & \text{otherwise,} \end{cases} \tag{11}$$

where  $d_i^*$  is the limited gradient used for the interpolation function (8), and  $d_{i\pm 1/2}$  are the two gradients on cell boundaries approximated in terms of the VIA moment by

$$d_{i-\frac{1}{2}} = \frac{\overline{V\phi}_i - \overline{V\phi}_{i-1}}{\Delta x} \quad \text{and} \quad d_{i+\frac{1}{2}} = \frac{\overline{V\phi}_{i+1} - \overline{V\phi}_i}{\Delta x}.$$

The minmod limiter [6] is defined as

$$\text{minmod}(a_1, a_2, a_3) = \begin{cases} s \cdot \min(|a_1|, |a_2|, |a_3|) & \text{if } s = \text{sign}(a_1) = \text{sign}(a_2) = \text{sign}(a_3), \\ 0 & \text{otherwise.} \end{cases}$$

We compute  $M$  with the formula given in [2,3],

$$M = \frac{2}{9}M_2(3 + 10M_2) \frac{\Delta x}{\Delta x + |d_{i-\frac{1}{2}}| + |d_{i+\frac{1}{2}}|}, \tag{12}$$

where  $M_2$  means the maximum absolute value of the second-order derivative over the computational domain. As the implementations in other methods, the optimal  $M_2$  in a TVB limiter is also somewhat case-dependent in our applications.

2.3. Time integration with the Runge–Kutta method

Provided the numerical solutions at step  $n$  ( $t = t^n$ ) for both moments,  $\overline{V}\phi_i^n$  and  $\overline{P}\phi_{i+1/2}^n$ , we consider the numerical procedure to update the moments to step  $n + 1$  ( $t = t^{n+1} = t^n + \Delta t$ ).

In a CIP-CSL scheme, computing the semi-Lagrangian solution to the PV moment involves a procedure to find out the departure point for each cell boundary, which is the solution at  $t^{n+1} = t^n + \Delta t$  to the initial value problem,

$$\begin{cases} \frac{dX}{dt} = -u(X, t); \\ X(t = t_0 = t^n) = X_0 = x_{i+\frac{1}{2}}, \end{cases} \tag{13}$$

for cell boundary point  $x_{i+1/2}$ .

In this paper, we use the Runge–Kutta method to solve (13). The third-order TVD Runge–Kutta method [16] reads as the following numerical steps for (13),

$$\begin{aligned} X_1 &= X_0 - u(X_0, t_0)\Delta t, \\ X_2 &= \frac{3}{4}X_0 + \frac{1}{4}X_1 - \frac{1}{4}u(X_1, t_1)\Delta t, \\ X_3 &= \frac{1}{3}X_0 + \frac{2}{3}X_2 - \frac{2}{3}u(X_2, t_2)\Delta t, \end{aligned} \tag{14}$$

or equivalently

$$\begin{aligned} X_1 &= X_0 - u(X_0, t_0)\Delta t, \\ X_2 &= X_0 - \frac{1}{4}(u(X_0, t_0) + u(X_1, t_1))\Delta t, \\ X_3 &= X_0 - \frac{1}{6}(u(X_0, t_0) + u(X_1, t_1) + 4u(X_2, t_2))\Delta t. \end{aligned} \tag{15}$$

From (1), we compute the PV according to the non-conservative form in which the flux is decomposed into an advection part and a non-advection part,

$$\frac{d\phi}{dt} = \frac{\partial\phi}{\partial t} + u \frac{\partial\phi}{\partial x} = -\phi \frac{\partial u}{\partial x}. \tag{16}$$

Considering the homogeneous part or the advection part in (16), we compute the PVs using the semi-Lagrangian solution at each substep of the Runge–Kutta time integration (14) as

$$\overline{P}\phi_{i+\frac{1}{2}}^{(l)} = \Phi_{i(X_l)}(X_l), \tag{17}$$

where  $l$  denotes the Runge–Kutta step, and  $l = 1, 2, 3$  for the third-order Runge–Kutta method. The location of the departure point  $X_l$  is the solution of (13) by the Runge–Kutta method, and  $\Phi_{i(X_l)}$  is the piecewise interpolation function constructed in terms of the moments at  $t = t^n$ , over the mesh cell that the departure point  $X_l$  falls in. The non-advection part in (16) is obtained by an integration along the trajectory  $\tau$ , and it can be approximated by the summation  $\widehat{\mathcal{D}}_{i+1/2} = -\Delta t \sum_{l'=0}^{l-1} \alpha_{l'} \Phi_{i(X_{l'})}(X_{l'}) \frac{\partial u}{\partial x}(X_0)$ , where  $\alpha_{l'}$  denotes the Runge–Kutta weight coefficients. The PV at the cell boundary of step  $n + 1$  is finally obtained as  $\overline{P}\phi_{i+1/2}^{n+1} = \overline{P}\phi_{i+1/2}^{(3)} + \widehat{\mathcal{D}}_{i+1/2}$ .

Concerning the computation of the VIA moment, we integrate (1) over  $[x_{i-1/2}, x_{i+1/2}]$ , yielding the following conservative formulation to update the VIA,

$$\frac{\partial \overline{V}\phi_i}{\partial t} = -\frac{1}{\Delta x_i} (\mathcal{F}_{i+\frac{1}{2}}(u, \phi) - \mathcal{F}_{i-\frac{1}{2}}(u, \phi)), \tag{18}$$

where  $\mathcal{F}(u, \phi)$  denotes the numerical flux consistent to  $(u\phi)$ . Rather than the exact integration of the interpolation function used in the original CIP-CSL schemes [20,37,28,29], an average numerical flux is evaluated from the PVs at all substeps of the Runge–Kutta integration computed in (17).

With PVs computed at each substep by the third-order TVD Runge–Kutta method (15), we approximate the numerical flux by

$$\mathcal{F}_{i+\frac{1}{2}}(u, \phi) \approx \widehat{\mathcal{F}}_{i+\frac{1}{2}} = \frac{\mathcal{F}\left(u(X_0), \overline{P\phi}_{i+\frac{1}{2}}^{(0)}\right) + \mathcal{F}\left(u(X_0), \overline{P\phi}_{i+\frac{1}{2}}^{(1)}\right) + 4\mathcal{F}\left(u(X_0), \overline{P\phi}_{i+\frac{1}{2}}^{(2)}\right)}{6}. \tag{19}$$

The VIA moment is then predicted by

$$\overline{v\phi}_i^{n+1} = \overline{v\phi}_i^n - \frac{\Delta t}{\Delta x_i} (\widehat{\mathcal{F}}_{i+\frac{1}{2}} - \widehat{\mathcal{F}}_{i-\frac{1}{2}}). \tag{20}$$

Note that we make use of the PVs sampled at the Runge–Kutta substeps along the trajectory for the computation of numerical flux in the present schemes, rather than the exact integral of the interpolation function for the numerical flux which is employed in the original CIP-CSL schemes. This provides us great convenience and efficiency, especially in multi-dimensional cases. Moreover, the following facts indicate that the third-order Runge–Kutta method with the CIP-CSL2 reconstruction gives a third-order accuracy to both PV and VIA.

For simplicity, we consider the linear scalar equation

$$\mathcal{L}(\phi) \equiv \frac{\partial \phi}{\partial t} + \frac{\partial(u\phi)}{\partial x} = 0, \tag{21}$$

where we assume  $u > 0$  is constant over the computational domain with a uniform grid spacing.

**Proposition 1.** *Let  $l = 3$  in (17) and use the CIP-CSL2 reconstruction, the semi-Lagrangian solution of the point value at cell boundary has third-order accuracy.*

**Proof.** From (17) with  $l = 3$ , we update the PV at  $x_{i+1/2}$  by

$$\overline{P\phi}_{i+\frac{1}{2}}^{n+1} = \Phi_i(X_3) = \Phi_i(x_{i+1/2} - u\Delta t) = 6\sigma(1 - \sigma)\overline{v\phi}_i^n + (1 - 4\sigma + 3\sigma^2)\overline{P\phi}_{i+\frac{1}{2}}^n - \sigma(2 - 3\sigma)\overline{P\phi}_{i-\frac{1}{2}}^n, \tag{22}$$

where  $\sigma = u\Delta t/\Delta x$  is the Courant number, and the CIP-CSL2 reconstruction (4) has been used.

The VIA  $\overline{v\phi}_i$  is approximated by third-order integration  $\overline{v\phi} \approx (\overline{P\phi}_{i-1/2} + \overline{P\phi}_{i-1/2} + 4\phi_i)/6$  over cell  $i$ , where  $\phi_i$  means the point value at cell center. Substituting above approximated VIA into (22), we express  $\overline{P\phi}_{i+\frac{1}{2}}^{n+1}$  in terms of the PVs at the  $n$ th step as

$$\overline{P\phi}_{i+\frac{1}{2}}^{n+1} = (1 - 3\sigma + 2\sigma^2)\overline{P\phi}_{i+\frac{1}{2}}^n - \sigma(1 - 2\sigma)\overline{P\phi}_{i-\frac{1}{2}}^n + 4\sigma(1 - \sigma)\phi_i^n. \tag{23}$$

Re-numbering the subscript by  $j \equiv i + 1/2, j - 1 \equiv i$  and  $j - 2 \equiv i - 1/2$ , we recast (23) into

$$\mathcal{L}_h(\overline{P\phi}) \equiv \overline{P\phi}_j^{n+1} - (1 - 3\sigma + 2\sigma^2)\overline{P\phi}_j^n + \sigma(1 - 2\sigma)\overline{P\phi}_{j-1}^n - 4\sigma(1 - \sigma)\phi_{j-2}^n = 0. \tag{24}$$

A Taylor expansion straightforwardly shows that

$$\mathcal{L}(\phi) - \mathcal{L}_h(\overline{P\phi}) = -\frac{\sigma(1 - 3\sigma + 2\sigma^2)\Delta x^3}{12} \frac{\partial^3 \phi}{\partial x^3} = \mathcal{O}(\Delta x^3, \Delta t^3). \tag{25}$$

It states the third-order accuracy of the numerical scheme.  $\square$

**Proposition 2.** *Let  $l = 3$  and use the CIP-CSL2 reconstruction, the numerical solution to the VIA computed by (19) and (20) has third-order accuracy.*

**Proof.** From (17), (19) and (20), the finite volume equation to update the VIA on the  $i$ th cell is written as

$$\begin{aligned} \overline{v}\phi_i^{n+1} &= \overline{v}\phi_i^n - \sigma \frac{\left(\overline{P}\phi_{i+\frac{1}{2}}^{(0)} + \overline{P}\phi_{i+\frac{1}{2}}^{(1)} + 4\overline{P}\phi_{i+\frac{1}{2}}^{(2)}\right) - \left(\overline{P}\phi_{i-\frac{1}{2}}^{(0)} + \overline{P}\phi_{i-\frac{1}{2}}^{(1)} + 4\overline{P}\phi_{i-\frac{1}{2}}^{(2)}\right)}{6}, \\ &= \overline{v}\phi_i^n + \sigma \left(-\overline{P}\phi_{i+\frac{1}{2}}^n + \overline{P}\phi_{i-\frac{1}{2}}^n\right) + \sigma^2 \left(-3\overline{v}\phi_i^n + 3\overline{v}\phi_{i-1}^n + 2\overline{P}\phi_{i+\frac{1}{2}}^n - \overline{P}\phi_{i-\frac{1}{2}}^n - \overline{P}\phi_{i-\frac{3}{2}}^n\right) \\ &\quad + \sigma^3 \left(2\overline{v}\phi_i^n - 2\overline{v}\phi_{i-1}^n - \overline{P}\phi_{i+\frac{1}{2}}^n + \overline{P}\phi_{i-\frac{3}{2}}^n\right). \end{aligned} \tag{26}$$

On the other hand, considering the Taylor expansion of  $\phi(x, t)$  about time  $t$  and (21), we have

$$\begin{aligned} \phi(x, t + \Delta t) &= \phi(x, t) + \Delta t \frac{\partial \phi}{\partial t} + \frac{\Delta t^2}{2!} \frac{\partial^2 \phi}{\partial t^2} + \frac{\Delta t^3}{3!} \frac{\partial^3 \phi}{\partial t^3} + \frac{\Delta t^4}{4!} \frac{\partial^4 \phi}{\partial t^4} + \dots \\ &= \phi(x, t) - u\Delta t \frac{\partial \phi}{\partial x} + u^2 \frac{\Delta t^2}{2!} \frac{\partial^2 \phi}{\partial x^2} - u^3 \frac{\Delta t^3}{3!} \frac{\partial^3 \phi}{\partial x^3} + u^4 \frac{\Delta t^4}{4!} \frac{\partial^4 \phi}{\partial x^4} + \dots \end{aligned} \tag{27}$$

We integrate (27) over  $[x_{i-1/2}, x_{i+1/2}]$ , and truncate the expansion at an order of  $\mathcal{O}(\Delta x^3, \Delta t^3)$

$$\overline{v}\phi_i^{n+1} = \overline{v}\phi_i^n - u \frac{\Delta t}{\Delta x} \left(\phi_{i+\frac{1}{2}} - \phi_{i-\frac{1}{2}}\right) + u^2 \frac{\Delta t^2}{2! \Delta x} \left(\frac{\partial \phi}{\partial x} \Big|_{i+\frac{1}{2}} - \frac{\partial \phi}{\partial x} \Big|_{i-\frac{1}{2}}\right) - u^3 \frac{\Delta t^3}{3! \Delta x} \left(\frac{\partial^2 \phi}{\partial x^2} \Big|_{i+\frac{1}{2}} - \frac{\partial^2 \phi}{\partial x^2} \Big|_{i-\frac{1}{2}}\right) + \mathcal{O}(\Delta x^3, \Delta t^3). \tag{28}$$

Considering the upwind direction for  $u > 0$ , one gets the followings with the CIP-CSL2 reconstruction (4),

$$\begin{aligned} \phi_{i+\frac{1}{2}} &\equiv \Phi_i(x_{i+\frac{1}{2}}), \quad \frac{\partial \phi}{\partial x} \Big|_{i+\frac{1}{2}} \equiv \frac{\partial \Phi_i}{\partial x}(x_{i+\frac{1}{2}}), \quad \frac{\partial^2 \phi}{\partial x^2} \Big|_{i+\frac{1}{2}} \equiv \frac{\partial^2 \Phi_i}{\partial x^2}(x_{i+\frac{1}{2}}), \\ \phi_{i-\frac{1}{2}} &\equiv \Phi_{i-1}(x_{i-\frac{1}{2}}), \quad \frac{\partial \phi}{\partial x} \Big|_{i-\frac{1}{2}} \equiv \frac{\partial \Phi_{i-1}}{\partial x}(x_{i-\frac{1}{2}}), \quad \frac{\partial^2 \phi}{\partial x^2} \Big|_{i-\frac{1}{2}} \equiv \frac{\partial^2 \Phi_{i-1}}{\partial x^2}(x_{i-\frac{1}{2}}). \end{aligned} \tag{29}$$

Expressing the interpolation function in the above relations explicitly using (4) and substituting the resulting expressions into (28), we immediately know that all the terms in (26) are identical to the leading terms in (28). This means that the finite volume formula (18) with (19) and (20) produces a truncation error of third-order.  $\square$

We should note that although the above conclusions are proved for constant velocity, they also applies to the case of variable velocity because the third-order Runge–Kutta method for the ordinary differential equation of the trajectory has a third-order accuracy only if the velocity is continuous.

For the convenience of further discussions and distinguishing the presented schemes from the existing ones, we refer to the third-order scheme with the slope parameter  $d_i$  approximated by (9) as CM<sup>2</sup>-FVM-SL3, a shorting of *CIP/multi-moment finite volume method based on semi-Lagrangian approach of third-order*, and the fourth-order scheme as CM<sup>2</sup>-FVM-SL4, where  $d_i$  is computed by (10).

### 2.4. Numerical examples

We computed some numerical examples of the scalar conservation laws to validate the proposed method for both linear and nonlinear cases. All experiments are computed with uniform grid and CFL number is about 0.4 except for the grid refinement tests. However, it is noted that the presented schemes are computationally stable even with a larger CFL number owing to the semi-Lagrangian nature.

We first solve the linear advection equation with constant velocity  $u = 1$ ,

$$\frac{\partial \phi}{\partial t} + \frac{\partial \phi}{\partial x} = 0. \tag{30}$$

**Example 2.1.** In order to evaluate the convergence rates of the schemes, we conducted grid-refinement experiments. A smooth distribution defined by



$$\phi(x, 0) = \sin(\pi x), \quad (0 \leq x \leq 2), \tag{31}$$

was transported by the one-dimensional advection equation with periodic boundary conditions. The number of mesh elements is doubly increased from 10 to 320 and the CFL number is fixed as 0.1.

The numerical errors measured by two kinds of norms defined as  $L_1 = \sum_{i=1}^I |\phi_i^e - \phi_i^n|/I$  and  $L_\infty = \max_{1 \leq i \leq I} (\phi_i^e - \phi_i^n)$  norms, where  $\phi^e$  is the exact solution. The convergence rates of the PV and VIA are shown in Tables 1 and 2. In this example, the slope parameter  $d$  was computed by (9) and (10) respectively in CM<sup>2</sup>-FVM-SL3 and CM<sup>2</sup>-FVM-SL4 without limiting.

It is observed that the CM<sup>2</sup>-FVM-SL3 has a third-order accuracy as the propositions suggest, while the CM<sup>2</sup>-FVM-SL4 has a fourth-order accuracy.

**Example 2.2.** As an example of capturing contact discontinuity, a square pulse was also computed. The square-pulse is given as

$$\phi(x, 0) = \begin{cases} 1 & \text{for } 0.8 \leq x \leq 1.2, \\ 0 & \text{otherwise,} \end{cases} \quad (0 \leq x \leq 2). \tag{32}$$

The numerical results using 100 mesh cells with  $M_2 = 0, 150$  and  $300$  in (12) at  $t = 4$  (2-period) are displayed in Figs. 2 and 3. Both CM<sup>2</sup>-FVM-SL3 and CM<sup>2</sup>-FVM-SL4 have produced symmetrical numerical solutions without numerical oscillation if  $M_2 = 0$ . However, there are significant differences between the two when the TVB bound  $M_2$  is increased. The second-order formula (9) gives a small slope at the cell center, and then

Table 1  
Numerical errors and convergence rate of the CM<sup>2</sup>-FVM-SL3 for the linear scalar equation  $\phi_t + \phi_x = 0$

Moment	Mesh size	$L_1$ error	$L_1$ order	$L_\infty$ error	$L_\infty$ order
PV	10	1.05e – 2	–	1.71e – 2	–
	20	1.37e – 3	2.94	2.20e – 3	2.96
	40	1.75e – 4	2.97	2.79e – 4	2.98
	80	2.21e – 5	2.99	3.50e – 5	2.99
	160	2.77e – 6	3.00	4.38e – 6	3.00
	320	3.48e – 7	2.99	5.47e – 7	3.00
VIA	10	1.07e – 2	–	1.65e – 2	–
	20	1.39e – 3	2.94	2.17e – 3	2.93
	40	1.75e – 4	2.99	2.75e – 4	2.98
	80	2.20e – 5	2.99	3.45e – 5	2.99
	160	2.75e – 6	3.00	4.32e – 6	3.00
	320	3.44e – 7	3.00	5.41e – 7	3.00

Table 2  
Numerical errors and convergence rate of the CM<sup>2</sup>-FVM-SL4 for the linear scalar equation  $\phi_t + \phi_x = 0$

Moment	Mesh size	$L_1$ error	$L_1$ order	$L_\infty$ error	$L_\infty$ order
PV	10	5.98e – 4	–	8.81e – 4	–
	20	3.43e – 5	4.12	5.22e – 5	4.08
	40	2.06e – 6	4.06	3.19e – 6	4.03
	80	1.27e – 7	4.02	1.98e – 7	4.01
	160	7.91e – 9	4.01	1.24e – 8	4.00
	320	4.94e – 10	4.00	7.74e – 10	4.00
VIA	10	5.73e – 4	–	8.85e – 4	–
	20	3.29e – 5	4.12	5.15e – 5	4.10
	40	2.01e – 6	4.03	3.15e – 6	4.03
	80	1.25e – 7	4.01	1.96e – 7	4.01
	160	7.80e – 9	4.00	1.22e – 8	4.01
	320	4.87e – 10	4.00	7.66e – 10	3.99

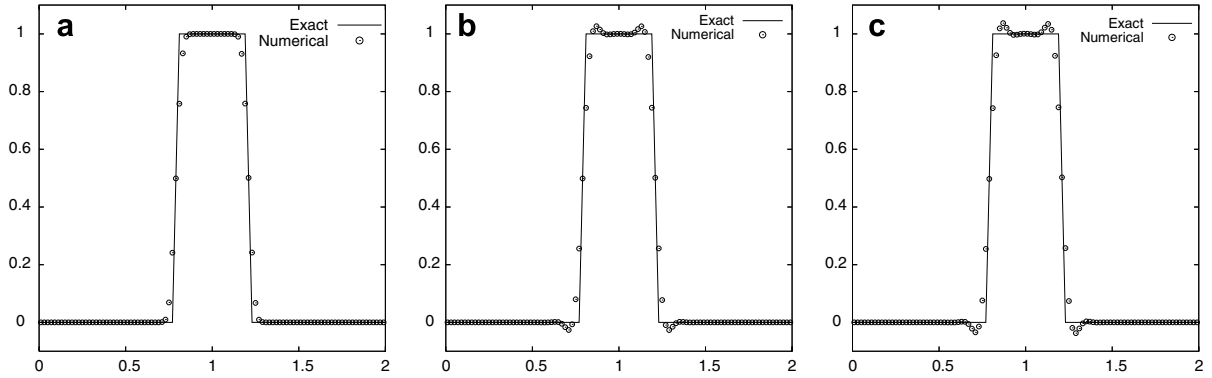


Fig. 2. Numerical results of CM<sup>2</sup>-FVM-SL3 for Example 2.2 at  $t = 4.0$  (2-period): (a)  $M_2 = 0$ ; (b)  $M_2 = 150$ ; and (c)  $M_2 = 300$ .

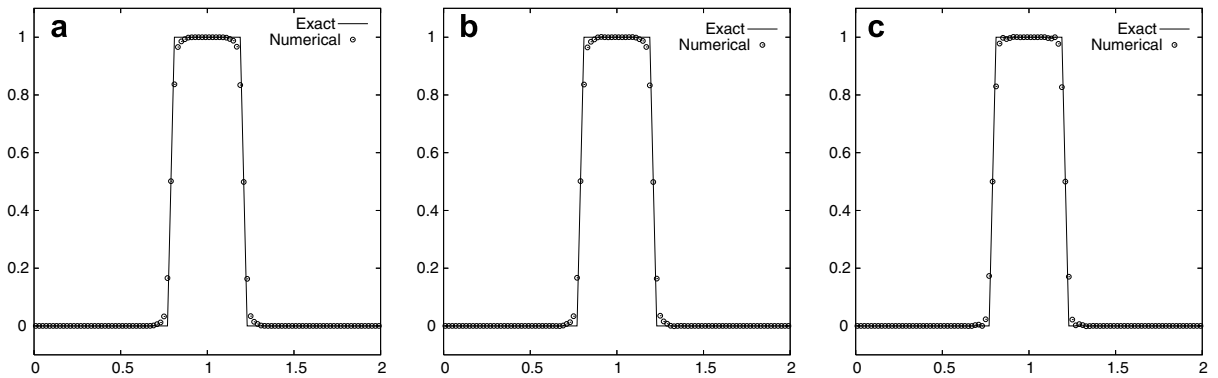


Fig. 3. Same as Fig. 2, but for CM<sup>2</sup>-FVM-SL4: (a)  $M_2 = 0$ ; (b)  $M_2 = 150$ ; and (c)  $M_2 = 300$ .

turns off the limiting. The fourth-order one (10) results in a much larger gradient that activates the slope limiter for all cases. The TVB limiter is apparently more effective for high-order reconstruction.

**Example 2.3.** In this example, we tested the schemes in capturing extrema of various smoothness [7]. The initial profile is given as

$$\phi(x + 0.5, 0) = \begin{cases} -x \sin(\frac{3}{2}\pi x^2) & \text{for } -1 \leq x \leq -\frac{1}{3}, \\ |\sin(2\pi x)| & \text{for } |\frac{1}{3}| \leq x, \\ 2x - 1 - \sin(3\pi x)/6 & \text{otherwise.} \end{cases} \quad (-1 \leq x \leq 1). \quad (33)$$

The initial profile was numerical transported up to  $t = 8$  (4-period) using 100 cells by both CM<sup>2</sup>-FVM-SL3 and CM<sup>2</sup>-FVM-SL4 with  $M_2 = 0, 150$  and  $300$ . The numerical solutions are shown in Fig. 4 and 5. As expected, the extrema are better resolved by both schemes when a larger  $M_2$  is used. The fourth-order scheme is overall superior to the third-order one.

We computed the inviscid Burgers equation as an example of scalar nonlinear conservation laws:

$$\frac{\partial u}{\partial t} + \frac{\partial(\frac{1}{2}u^2)}{\partial x} = 0. \quad (34)$$

The PV is solved by the advection form

$$\frac{du}{dt} = \frac{\partial u}{\partial t} + a(u) \frac{\partial u}{\partial x} = 0, \quad (35)$$

where  $a(u) = u$  is the characteristics velocity.

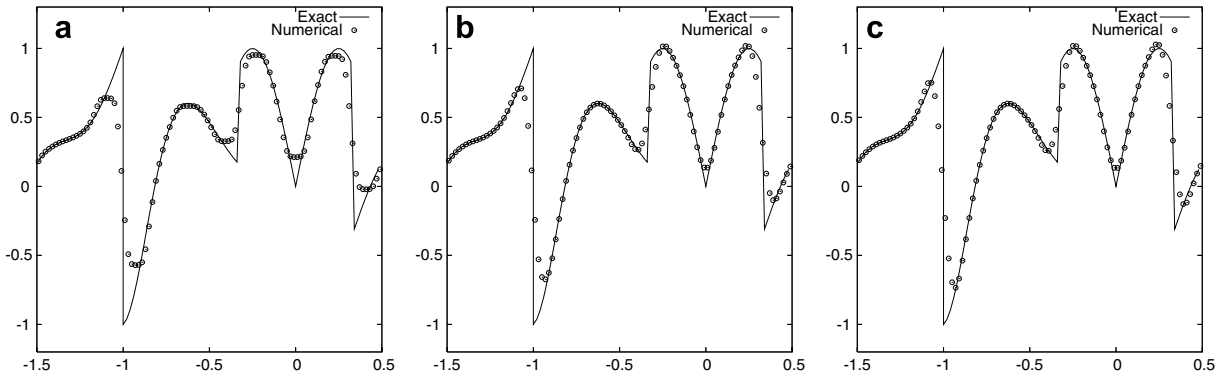


Fig. 4. Numerical results of CM<sup>2</sup>-FVM-SL3 for Example 2.3 at  $t = 8.0$  (4-period): (a)  $M_2 = 0$ ; (b)  $M_2 = 150$ ; and (c)  $M_2 = 300$ .

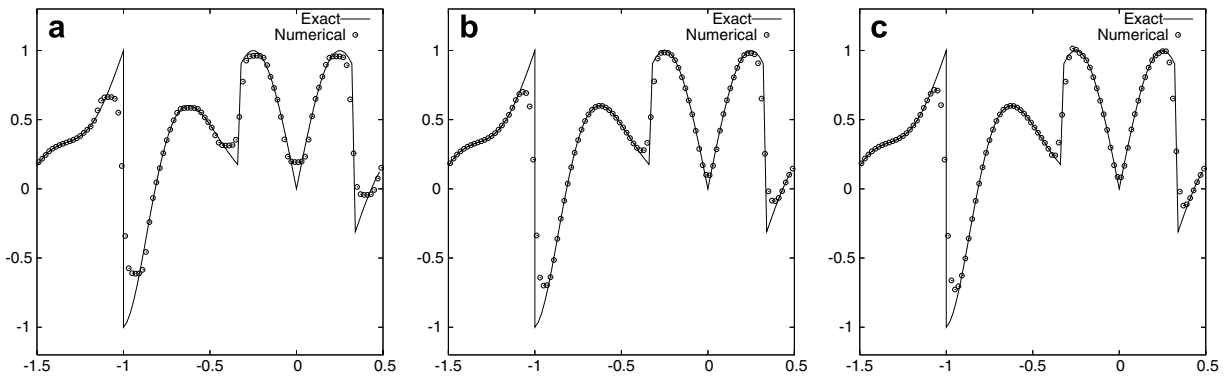


Fig. 5. Same as Fig. 4, but for CM<sup>2</sup>-FVM-SL4: (a)  $M_2 = 0$ ; (b)  $M_2 = 150$ ; and (c)  $M_2 = 300$ .

The trajectory passing through cell boundary is solved with a characteristic velocity evaluated by

$$a(u)_{i+\frac{1}{2}} = \begin{cases} \text{sgn}(\max) \cdot \max \left( |\overline{p}u_{i+\frac{1}{2}}|, |\overline{v}u_{i-1}|, |\overline{v}u_{i+1}| \right) & \text{for discontinuity,} \\ \overline{p}u_{i+\frac{1}{2}} & \text{otherwise.} \end{cases} \quad (36)$$

Our numerical experiments show that (36) not only avoids effectively the “entropy problem” at sonic points but also works well in suppressing numerical oscillations.

Same as in the linear cases, the numerical flux for updating VIA is obtained by

$$\widehat{\mathcal{F}}_{i+\frac{1}{2}} = \frac{\frac{1}{2}(\overline{p}u_{i+\frac{1}{2}}^{(0)})^2 + \frac{1}{2}(\overline{p}u_{i+\frac{1}{2}}^{(1)})^2 + 2(\overline{p}u_{i+\frac{1}{2}}^{(2)})^2}{6}, \quad (37)$$

and the VIAs are updated by

$$\overline{v}u_i^{n+1} = \overline{v}\phi_i^n - \frac{\Delta t}{\Delta x_i} \left( \widehat{\mathcal{F}}_{i+\frac{1}{2}} - \widehat{\mathcal{F}}_{i-\frac{1}{2}} \right). \quad (38)$$

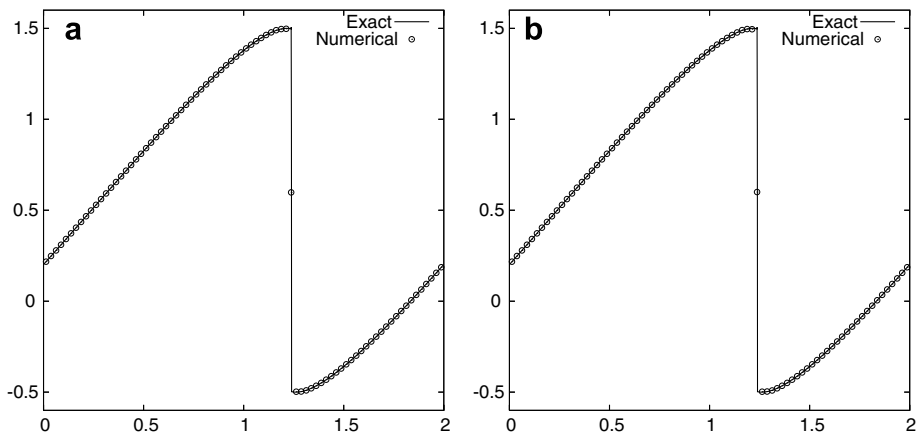
**Example 2.4.** We evaluated the convergence rates of the schemes for the nonlinear Burgers equation with the numerical test in [23,12]. The initial condition is given as

$$u(x, 0) = 0.5 + \sin(\pi x), \quad (0 \leq x \leq 2). \quad (39)$$

Table 3

Numerical errors and convergence rate for the nonlinear scalar equation  $u_t + (u^2/2)_x = 0$ 

Scheme	Mesh size	$L_1$ error	$L_1$ order	$L_\infty$ error	$L_\infty$ order
CM <sup>2</sup> -FVM-SL3	10	7.94e-3	–	2.64e-2	–
	20	7.31e-4	3.44	4.05e-3	2.70
	40	9.22e-5	2.99	5.24e-4	2.95
	80	1.14e-5	3.02	5.94e-5	3.14
	160	1.07e-6	3.41	4.87e-6	3.61
	320	9.98e-8	3.42	4.51e-7	3.43
CM <sup>2</sup> -FVM-SL4	10	3.45e-3	–	1.14e-2	–
	20	1.83e-4	4.00	1.04e-3	3.45
	40	1.61e-5	4.00	9.43e-5	3.46
	80	8.03e-7	4.60	5.08e-6	4.21
	160	5.01e-8	4.28	3.33e-7	3.93
	320	2.31e-9	4.09	1.64e-8	4.34

Fig. 6. Numerical results of Example 2.4 at  $t = 1.5/\pi$ : (a) CM<sup>2</sup>-FVM-SL3 and (b) CM<sup>2</sup>-FVM-SL4.

Due to the nonlinearity, the discontinuous solution (shock wave) is fully developed around  $t = 2/\pi$ . We solved the Burgers equation up to  $t = 0.5/\pi$  when the solution is still smooth. The numerical errors measured in both  $L_1$  and  $L_\infty$  norms and the convergence rates of the CM<sup>2</sup>-FVM-SL3 and CM<sup>2</sup>-FVM-SL4 for VIA are shown in Table 3. The expected convergence rates of both schemes are verified again for the nonlinear case.

Moreover, we continued the calculation with 80 mesh cells until  $t = 1.5/\pi$  and obtained a well developed shock wave. The numerical solutions of the CM<sup>2</sup>-FVM-SL3 and CM<sup>2</sup>-FVM-SL4 are shown in Fig. 6. The shock discontinuity is well resolved by both schemes without numerical oscillations. The TVB parameter in this test is set as  $M = 7/\Delta x$ . It reflects the fact that the numerical derivatives are grid-spacing dependent. The parameter  $M$  is pre-determined in a manner dependent on the grid resolution in this test. It is observed at least for this test that  $M = 7/\Delta x$  does not trigger the minmod limiter, otherwise a lower convergence rate would be resulted.

### 3. The Euler conservation laws

In this section, we implement the CIP/MM FVM to the inviscid Euler conservation laws. We make use of the strict hyperbolicity of the Euler equations, so the numerical procedure can be extended to system of equations by computing the semi-Lagrangian solutions in terms of the characteristics. The numerical fluxes, which are required in the computation of the VIAs of the conservative variables, are approximated by using the semi-

Lagrangian solutions of the characteristic variables. In the computation of the Euler equations, we use the third-order TVD Runge–Kutta method for time integration again.

### 3.1. The one-dimensional Euler equations

The conservative form of the one-dimensional Euler equations, which describe the dynamics of inviscid gas, are given as follows:

$$\frac{\partial \mathbf{U}}{\partial t} + \frac{\partial \mathbf{F}}{\partial x} = 0, \quad \mathbf{U} = \begin{bmatrix} \rho \\ \rho u \\ e \end{bmatrix}, \quad \mathbf{F} = \begin{bmatrix} \rho u \\ \rho u^2 + p \\ u(e + p) \end{bmatrix}, \tag{40}$$

where  $\mathbf{U}$  is the vector of conservative variables and  $\mathbf{F}$  is the vector of inviscid fluxes. Denoted by  $\rho$  is the density,  $u$  the velocity,  $e$  the total energy and  $p$  the pressure that is obtained by the equation of state for the perfect gas  $p = (e - \rho u^2/2)(\gamma - 1)$ . The ratio of the specific heats  $\gamma$  is specified as 1.4 in this paper.

From (40), we can obtain the linearized Euler equations about the primitive variables  $\mathbf{W}$  by freezing the jacobian matrix  $\mathbf{A}$ ,

$$\frac{\partial \mathbf{W}}{\partial t} + \mathbf{A} \frac{\partial \mathbf{W}}{\partial x} = 0, \quad \mathbf{W} = \begin{bmatrix} \rho \\ u \\ p \end{bmatrix}, \quad \mathbf{A} = \begin{bmatrix} u & \rho & 0 \\ 0 & u & \frac{1}{\rho} \\ 0 & \rho c^2 & u \end{bmatrix}. \tag{41}$$

Considering the hyperbolicity, one can consider the following decomposition to diagonalize  $\mathbf{A}$ , i.e.

$$\mathbf{A} = \mathbf{R} \mathbf{\Lambda} \mathbf{L},$$

where  $\mathbf{\Lambda}$  is the diagonal matrix of the eigenvalues, whose non-zero diagonal elements are the characteristic speeds denoted by  $\lambda_1 = u$ ,  $\lambda_2 = u + c$  and  $\lambda_3 = u - c$ , respectively.  $\mathbf{L}$  is the matrix of the left eigenvectors (inverse matrix of right eigenvectors  $\mathbf{R}$ , i.e.  $\mathbf{L} = \mathbf{R}^{-1}$ ), and  $c = \sqrt{\gamma p / \rho}$  is the sound speed.

Eq. (41) is then recast into the characteristic form,

$$\mathbf{L} \frac{\partial \mathbf{W}}{\partial t} + \mathbf{\Lambda} \mathbf{L} \frac{\partial \mathbf{W}}{\partial x} = 0, \quad \mathbf{\Lambda} = \begin{bmatrix} u & 0 & 0 \\ 0 & u + c & 0 \\ 0 & 0 & u - c \end{bmatrix}, \quad \mathbf{L} = \begin{bmatrix} 1 & 0 & -\frac{1}{c^2} \\ 0 & 1 & \frac{1}{\rho c} \\ 0 & 1 & -\frac{1}{\rho c} \end{bmatrix}. \tag{42}$$

We, from (42), have a decoupled system for the characteristic variables (or the Riemann invariants) as,

$$d\rho - \frac{1}{c^2} dp = 0, \quad \text{on } \mathcal{C}_1(X_0) : \frac{dx}{dt} = \lambda_1 = u; \quad x(t = t_0) = X_0, \tag{43a}$$

$$du + \frac{1}{\rho c} dp = 0, \quad \text{on } \mathcal{C}_2(X_0) : \frac{dx}{dt} = \lambda_2 = u + c; \quad x(t = t_0) = X_0, \tag{43b}$$

$$du - \frac{1}{\rho c} dp = 0, \quad \text{on } \mathcal{C}_3(X_0) : \frac{dx}{dt} = \lambda_3 = u - c; \quad x(t = t_0) = X_0. \tag{43c}$$

So, the primitive variables at  $X_0$  can be found by the relations below,

$$\rho(X_0) - \rho(X(\mathcal{C}_1)) - \frac{1}{c^2} \{p(X_0) - p(X(\mathcal{C}_1))\} = 0, \tag{44a}$$

$$u(X_0) - u(X(\mathcal{C}_2)) + \frac{1}{\rho c} \{p(X_0) - p(X(\mathcal{C}_2))\} = 0, \tag{44b}$$

$$u(X_0) - u(X(\mathcal{C}_3)) - \frac{1}{\rho c} \{p(X_0) - p(X(\mathcal{C}_3))\} = 0, \tag{44c}$$

where  $X(\mathcal{C}_1)$ ,  $X(\mathcal{C}_2)$  and  $X(\mathcal{C}_3)$  indicate the points on the characteristic curves  $\mathcal{C}_1$ ,  $\mathcal{C}_2$  and  $\mathcal{C}_3$ , respectively.

3.2. The multi-moment discretization

Two types of moments, i.e. the PV at the cell boundary and the VIA over the cell volume, are defined and treated as the predicted variables for the primitive variables  $\mathbf{W}$ . The PVs and VIAs of  $\mathbf{W}$ , shown in Fig. 7, are defined as

$$\overline{P\mathbf{W}}_{i+\frac{1}{2}} = \mathbf{W}\left(x_{i+\frac{1}{2}}, t\right), \tag{45}$$

and

$$\overline{V\mathbf{W}}_i = \frac{1}{\Delta x_i} \int_{x_{i-\frac{1}{2}}}^{x_{i+\frac{1}{2}}} \mathbf{W}(x, t) dx. \tag{46}$$

The departure points  $X(\mathcal{C}_m)$ ,  $m = 1, 2, 3$ , of cell boundary  $x = x_{i+1/2}$  are obtained by solving the trajectory equations along the three characteristic curves,

$$\begin{cases} \frac{dX}{dt} = -\lambda_m(X, t), \\ X(t = t_0) = X_0 = x_{i+\frac{1}{2}}; \end{cases} \quad m = 1, 2, 3. \tag{47}$$

We solve (47) using the third-order TVD Runge–Kutta method, which reads

$$\begin{cases} X_1(\mathcal{C}_m) = X_0 - \lambda_m(X_0, t_0)\Delta t, \\ X_2(\mathcal{C}_m) = \frac{3}{4}X_0 + \frac{1}{4}X_1(\mathcal{C}_m) - \frac{1}{4}\lambda_m(X_0, t_1)\Delta t, \quad \text{for } m = 1, 2, 3; \\ X_3(\mathcal{C}_m) = \frac{1}{3}X_0 + \frac{2}{3}X_2(\mathcal{C}_m) - \frac{2}{3}\lambda_m(X_0, t_2)\Delta t, \end{cases} \tag{48}$$

where  $\mathcal{C}_m$  denotes the  $m$ th characteristic curve, defined by (47).

Consequently, by solving linear-system (44a)–(44c) for primitive variables  $(\rho, u, p)$  along characteristic curves, we have

$$\overline{P\rho}_{i+\frac{1}{2}}^{(l)} = \frac{1}{2} \left\{ \mathcal{P}(X_l(\mathcal{C}_2)) + \mathcal{P}(X_l(\mathcal{C}_3)) + \overline{P\rho}_{i+\frac{1}{2}}^{(l-1)} \overline{Pc}_{i+\frac{1}{2}}^{(l-1)} \{ \mathcal{U}(X_l(\mathcal{C}_2)) - \mathcal{U}(X_l(\mathcal{C}_3)) \} \right\}, \tag{49a}$$

$$\overline{Pu}_{i+\frac{1}{2}}^{(l)} = \frac{1}{2} \left\{ \mathcal{U}(X_l(\mathcal{C}_2)) + \mathcal{U}(X_l(\mathcal{C}_3)) + \frac{1}{\overline{P\rho}_{i+\frac{1}{2}}^{(l-1)} \overline{Pc}_{i+\frac{1}{2}}^{(l-1)}} \{ \mathcal{P}(X_l(\mathcal{C}_2)) - \mathcal{P}(X_l(\mathcal{C}_3)) \} \right\}, \tag{49b}$$

$$\overline{P\rho}_{i+\frac{1}{2}}^{(l)} = \mathcal{R}(X_l(\mathcal{C}_1)) + \frac{1}{(\overline{Pc}_{i+\frac{1}{2}}^{(l-1)})^2} \{ \overline{Pp}_{i+\frac{1}{2}}^{(l)} - \mathcal{P}(X_l(\mathcal{C}_1)) \}, \tag{49c}$$

where  $\mathcal{R}(x)$ ,  $\mathcal{U}(x)$  and  $\mathcal{P}(x)$  represent the CIP-CSL reconstructions for  $\rho$ ,  $u$  and  $p$ , respectively. Thus,  $\mathcal{R}(X_l(\mathcal{C}_m))$ ,  $\mathcal{U}(X_l(\mathcal{C}_m))$  and  $\mathcal{P}(X_l(\mathcal{C}_m))$  denote the semi-Lagrangian solutions along the trajectories defined by characteristic curve  $\mathcal{C}_m$  for the Runge–Kutta substeps ( $l = 1, 2, 3$ ).

The characteristic velocities  $\lambda_m(X_0, t_l)$  at each Runge–Kutta substep ( $l = 0, 1, 2$ ) are retrieved from the PVs of the primitive variables computed by (49a)–(49c), and then used in (48).

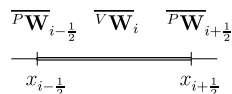


Fig. 7. The locations of the moments for the one-dimensional Euler equations on cell  $i$ .

The PVs of the primitive variables at the cell boundary  $x = x_{i+1/2}$  of step  $n + 1$  are found directly by

$$\overline{\rho}^{n+1}_{i+\frac{1}{2}} = \overline{\rho}^{(3)}_{i+\frac{1}{2}}, \tag{50}$$

$$\overline{u}^{n+1}_{i+\frac{1}{2}} = \overline{u}^{(3)}_{i+\frac{1}{2}}, \tag{51}$$

$$\overline{p}^{n+1}_{i+\frac{1}{2}} = \overline{p}^{(3)}_{i+\frac{1}{2}}. \tag{52}$$

Analogous to the case of the scalar conservation law, the VIAs of the conservative variables  $\mathbf{U}$  on cell  $i$  are updated by integrating (40) over  $[x_{i-1/2}, x_{i+1/2}]$ , which results in a finite volume formulation,

$$\overline{\mathbf{U}}_i^{n+1} = \overline{\mathbf{U}}_i^n - \frac{\Delta t}{\Delta x_i} \left( \widehat{\mathcal{F}}_{i+\frac{1}{2}} - \widehat{\mathcal{F}}_{i-\frac{1}{2}} \right), \tag{53}$$

where the numerical fluxes computed by using the PVs of the primitive variables at the substeps of the Runge–Kutta integration scheme (15), i.e.

$$\widehat{\mathcal{F}}_{i+\frac{1}{2}} = \frac{\mathcal{F}_{i+\frac{1}{2}}^{(0)} \left( \overline{\mathbf{W}}_{i+\frac{1}{2}}^{(0)} \right) + \mathcal{F}_{i+\frac{1}{2}}^{(1)} \left( \overline{\mathbf{W}}_{i+\frac{1}{2}}^{(1)} \right) + 4\mathcal{F}_{i+\frac{1}{2}}^{(2)} \left( \overline{\mathbf{W}}_{i+\frac{1}{2}}^{(2)} \right)}{6}. \tag{54}$$

In the whole numerical procedure, we assume that the relations of the continuous physical variables apply also to the PVs and VIAs, such as,

$$\overline{u} = \overline{\rho u} / \overline{\rho}, \quad \overline{p} = (\overline{v}e - \overline{\rho^v u^2} / 2)(\gamma - 1), \quad \text{and} \quad \overline{p}e = \overline{p} / (\gamma - 1) + \overline{\rho^p u^2} / 2.$$

#### 4. Numerical examples for the Euler equations

In this section, we report some benchmark tests that have been widely used to evaluate numerical schemes for the one-dimensional Euler equations. We denote the maximum CFL number in terms of the largest characteristic velocity over all computational time and mesh cells as  $\text{CFL}_{\max}$ . Our numerical experiments show that the present method is computational stable for the Euler equations only if  $\text{CFL}_{\max}$  is less than 0.8. In all tests in this paper, the time step is chosen so that  $\text{CFL}_{\max}$  is about 0.4.

Numerical tests were conducted with both the third-order scheme (CM<sup>2</sup>-FVM-SL3) and the fourth-order scheme (CM<sup>2</sup>-FVM-SL4) as mentioned before. The TVB slope limiting was implemented and the differences in the numerical results from different limiting parameters are shown.

##### 4.1. Advection of density perturbation [12]

In order to evaluate the convergence rate of the proposed schemes, we computed the Euler equations with gradually refined grids. The initial condition [12] for density, velocity and pressure are specified, respectively, as  $\rho_0 = 1 + 0.2\sin(\pi x)$ ,  $u_0 = 1$ ,  $p_0 = 1$ . The computational domain is over  $[0, 2]$  with periodic boundary conditions. These configuration produces an advection transport of the initial density perturbations. The exact solution of density is found as  $\rho(x, t) = 1 + 0.2\sin(\pi(x - t))$ ,  $u(x, t) = p(x, t) = 1$ .

The grid resolutions were doubly refined from 10 to 320. The  $L_1$  and  $L_\infty$  errors in the numerical results of density at  $t = 2$  and the corresponding convergence rates are summarized in Table 4. Same as in the pure advection cases, we have obtained the expected orders of accuracy for the Euler equations with variable characteristic velocities. Furthermore, we can find that the present schemes produce numerical results with accuracies competitive to those of the HWENO scheme in [12].

##### 4.2. Sod's problem [19]

Its perhaps the most widely used benchmark test for one-dimensional Euler equations. A 1D shock tube problem is configured with a diaphragm that initially separates the compressible ideal gas in the two states as follows:

Table 4

Numerical errors and convergence rate of the density  $\rho$  for the Euler Eq. (40) with initial conditions  $\rho_0 = 1 + 0.2\sin(\pi x)$  and  $u_0 = p_0 = 1$

Scheme	Mesh size	$L_1$ error	$L_1$ order	$L_\infty$ error	$L_\infty$ order
CM <sup>2</sup> -FVM-SL3	10	2.13e-3	–	3.30e-3	–
	20	2.77e-4	2.94	4.44e-4	2.89
	40	3.51e-5	2.98	5.50e-5	3.01
	80	4.40e-6	3.00	6.91e-6	2.99
	160	5.51e-7	3.00	8.65e-7	3.00
	320	6.89e-8	3.00	1.08e-7	3.00
CM <sup>2</sup> -FVM-SL4	10	1.15e-4	–	1.77e-4	–
	20	6.58e-6	4.13	1.03e-5	4.10
	40	4.02e-5	4.03	6.31e-7	4.03
	80	2.50e-8	4.01	3.92e-8	4.01
	160	1.56e-9	4.00	2.45e-9	4.00
	320	9.75e-11	4.00	1.53e-10	4.00

$$(\rho_0, u_0, p_0) = \begin{cases} (1, 0, 1) & \text{for } 0 \leq x \leq 0.5, \\ (0.125, 0, 0.1) & \text{otherwise,} \end{cases} \quad (0 \leq x \leq 1). \tag{55}$$

We carried out the calculations on 100 mesh cells until  $t = 0.2$ . The numerical results of CM<sup>2</sup>-FVM-SL3 and CM<sup>2</sup>-FVM-SL4 are shown in Figs. 8 and 9. The shock front and contact discontinuity are captured with correct locations and satisfactory sharpness. In this numerical test, we specified  $M_2 = 0$  in (12). The numerical results of both CM<sup>2</sup>-FVM-SL3 and CM<sup>2</sup>-FVM-SL4 look competitive to those of the DG method in [3], where

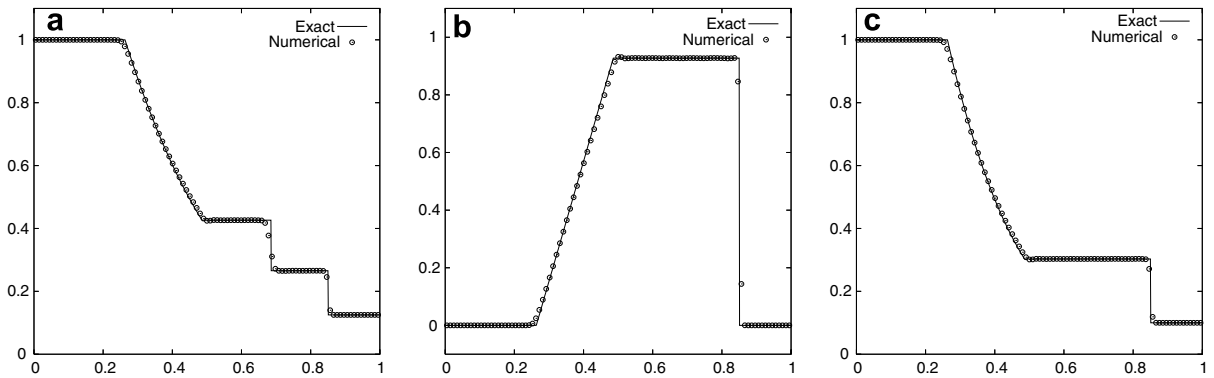


Fig. 8. Numerical results of CM<sup>2</sup>-FVM-SL3 for Sod's problem at  $t = 0.2$ : (a) density; (b) velocity; and (c) pressure.

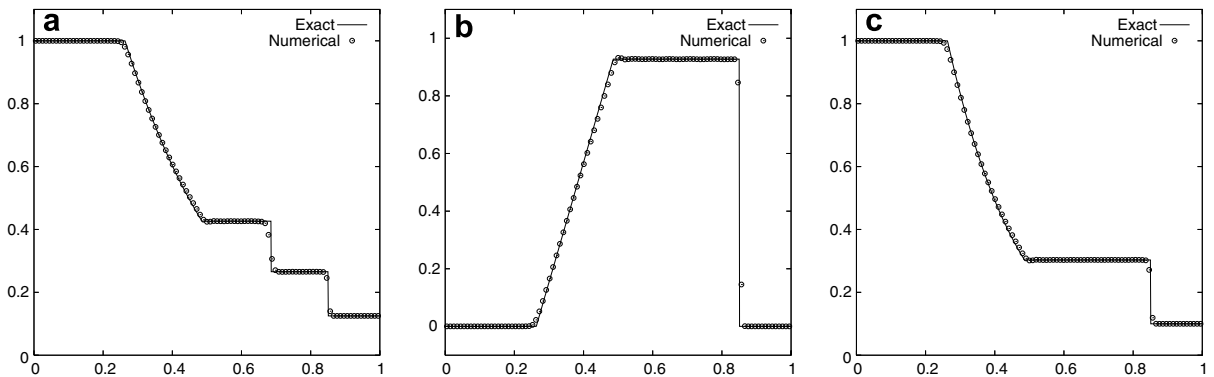


Fig. 9. Numerical results of CM<sup>2</sup>-FVM-SL4 for Sod's problem at  $t = 0.2$ : (a) density; (b) velocity; and (c) pressure.



a similar TVB limiting was also used to control the numerical oscillations, and tuning  $M_2$  makes significant difference in the computational outcomes.

4.3. Lax’s problem [10]

Another numerical test with stronger shock and contact discontinuity, namely Lax’s problem [10], is characterized by the following initial conditions,

$$(\rho_0, u_0, p_0) = \begin{cases} (0.445, 0.698, 3.528) & \text{for } 0 \leq x \leq 0.5, \\ (0.5, 0, 0.571) & \text{otherwise,} \end{cases} \quad (0 \leq x \leq 1). \tag{56}$$

We used 100 mesh cells. The numerical results at  $t = 0.13$  are shown in Figs. 10 and 11. Again, the numerical solutions of shock, contact discontinuity and expansion fan are obtained with a satisfactory resolution, even compared to those from the DG method reported in [3].

4.4. Extremely strong shock wave [32]

In this test, strong shock wave is generated by an extremely high pressure in the initial conditions,

$$(\rho_0, u_0, p_0) = \begin{cases} (1, 0, 10^{10}) & \text{for } 0 \leq x \leq 0.5, \\ (0.125, 0, 0.1) & \text{otherwise,} \end{cases} \quad (0 \leq x \leq 1). \tag{57}$$

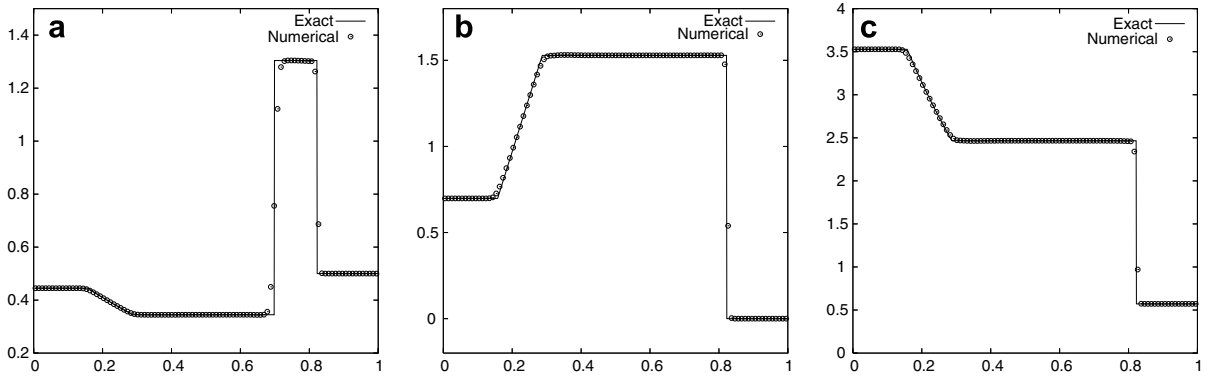


Fig. 10. Numerical results of CM<sup>2</sup>-FVM-SL3 for Lax’s problem at  $t = 0.13$ : (a) density; (b) velocity; and (c) pressure.

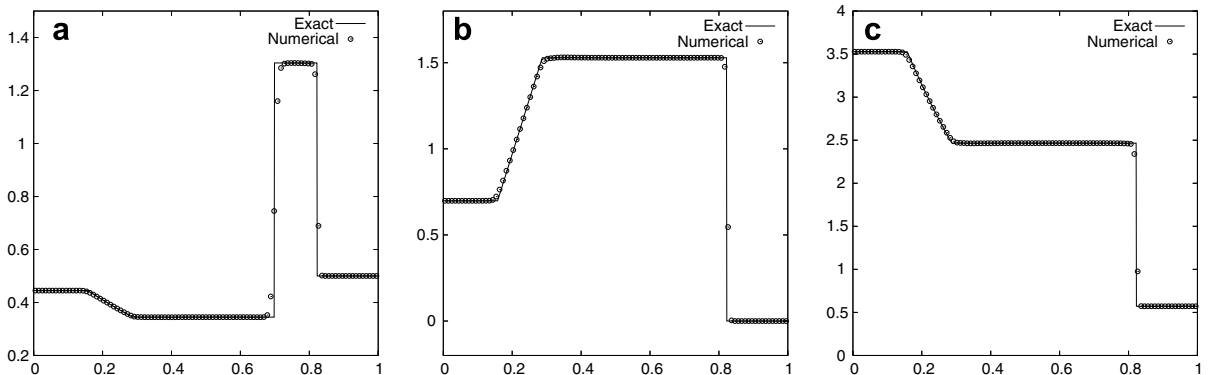


Fig. 11. Numerical results of CM<sup>2</sup>-FVM-SL4 for Lax’s problem at  $t = 0.13$ : (a) density; (b) velocity; and (c) pressure.

In this example, the characteristic velocities  $\lambda_m(m = 1, 2, 3)$  are very large. We compute the characteristic velocities at each cell boundary by a weighted averaging between the values in terms of the PVs ( $\overline{P\lambda}_m$ ) and the values evaluated from the Roe’s average [13] ( $\overline{Roe\lambda}_m$ ) based on the VIAs of the two neighboring cells as

$$\hat{\lambda}_m = \beta \overline{P\lambda}_m + (1 - \beta) \overline{Roe\lambda}_m. \tag{58}$$

In this example, the weight parameter is  $\beta = 0.5$ .

We carried out the calculation over 200 mesh cells. The numerical results at  $t = 2.5 \times 10^{-6}$  are shown in Figs. 12 and 13. Due to the numerical conservativeness of the VIAs of the conservative variables, the shock with large jumps in both velocity and pressure were computed with correct locations. The numerical solutions look very satisfactory in regard to numerical diffusion and spurious oscillations.

4.5. Stationary contact discontinuity

A stationary contact discontinuity was examined with initial conditions as follows:

$$(\rho_0, u_0, p_0) = \begin{cases} (1.4, 0, 1) & \text{for } 0 \leq x \leq 0.5, \\ (1, 0, 1) & \text{otherwise,} \end{cases} \quad (0 \leq x \leq 1). \tag{59}$$

The discontinuity in density remains stationary, but poses a challenging problem for some existing high resolution schemes, for example, a smeared discontinuity is produced by the flux vector splitting method [22]. Shown in Fig. 14, numerical solutions identical to the exact ones have been obtained by both CM<sup>2</sup>-FVM-SL3 and CM<sup>2</sup>-FVM-SL4.

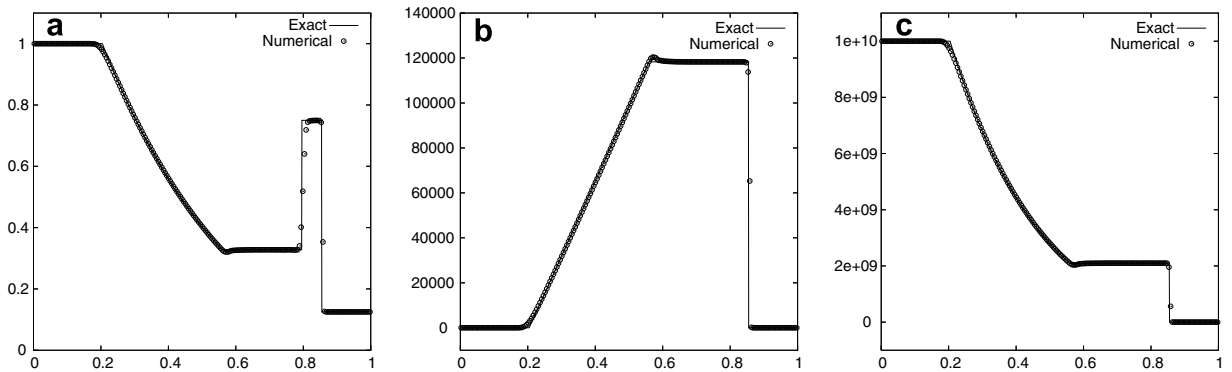


Fig. 12. Numerical results of CM<sup>2</sup>-FVM-SL3 for extremely strong shock wave at  $t = 2.5 \times 10^{-6}$ : (a) density; (b) velocity; and (c) pressure.

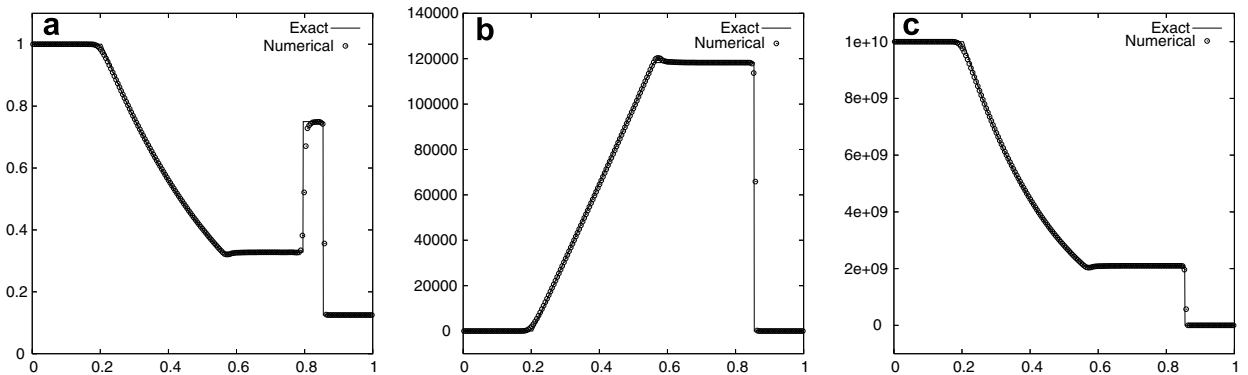


Fig. 13. Numerical results of CM<sup>2</sup>-FVM-SL4 for extremely strong shock wave at  $t = 2.5 \times 10^{-6}$ : (a) density; (b) velocity; and (c) pressure.

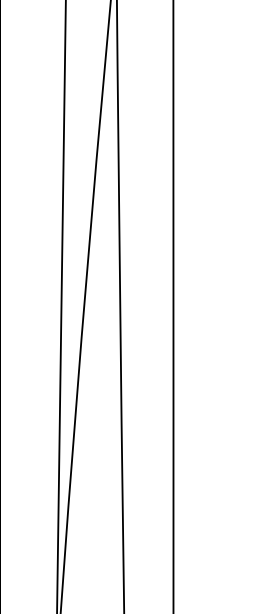


Fig. 14. Numerical

#### 4.6. Shock-turbulence

As in [18], the initial conditions

$$(\rho_0, u_0, p_0)$$

In this problem

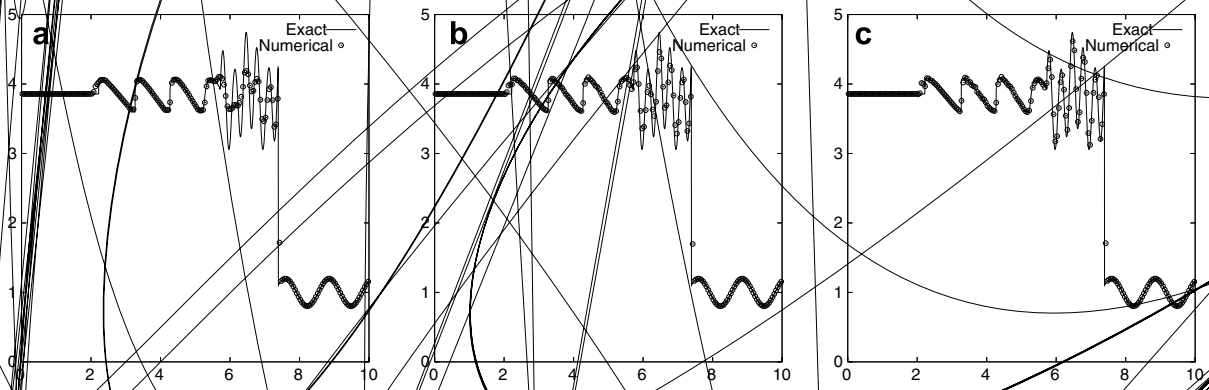


Fig. 16. Numerical results of CMF-FVM-SL4 for shock-turbulence interaction at  $t = 1.8$ . Mesh number is 200: (a)  $M_2 = 0$ ; (b)  $M_2 = 100$ ; and (c)  $M_2 = 200$ .

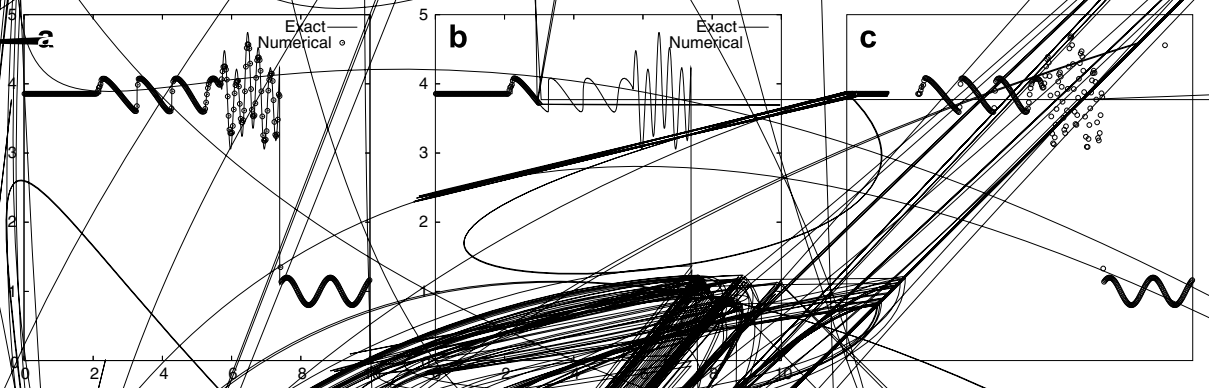


Fig. 17. Same as Fig. 16, but with a mesh number of 100: (a)  $M_2 = 0$ ; (b)  $M_2 = 100$ ; and (c)  $M_2 = 200$ .

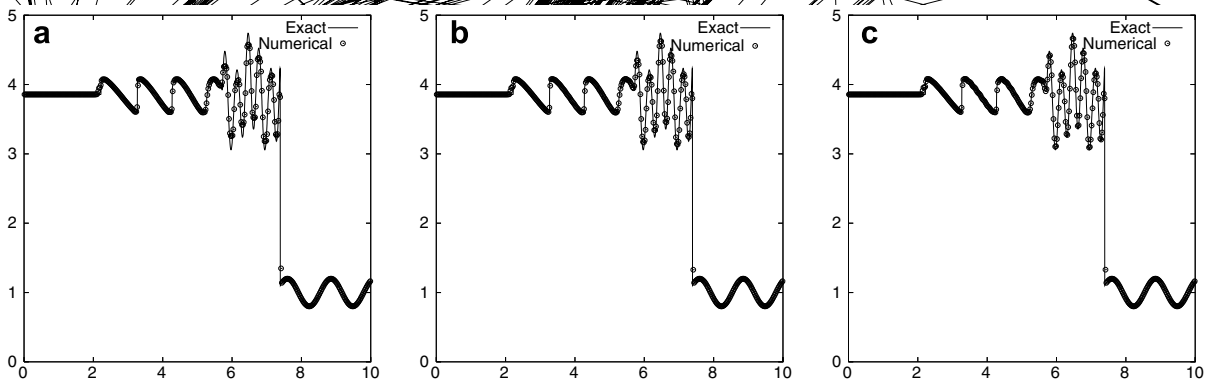


Fig. 18. Same as Fig. 16, but the mesh number is 400: (a)  $M_2 = 0$ ; (b)  $M_2 = 100$ ; and (c)  $M_2 = 200$ .

#### 4.7. Two interacting blast waves [27]

Finally, we computed two interacting blast waves suggested in [27]. The initial conditions were given by

$$(p, u, P_0) = \begin{cases} (1, 0, 1000) & \text{for } 0 \leq x \leq 0.1, \\ (1, 0, 0.01) & \text{for } 0.1 \leq x \leq 0.9, \quad (0 \leq x \leq 1). \\ (1, 0, 100) & \text{otherwise,} \end{cases} \quad (61)$$

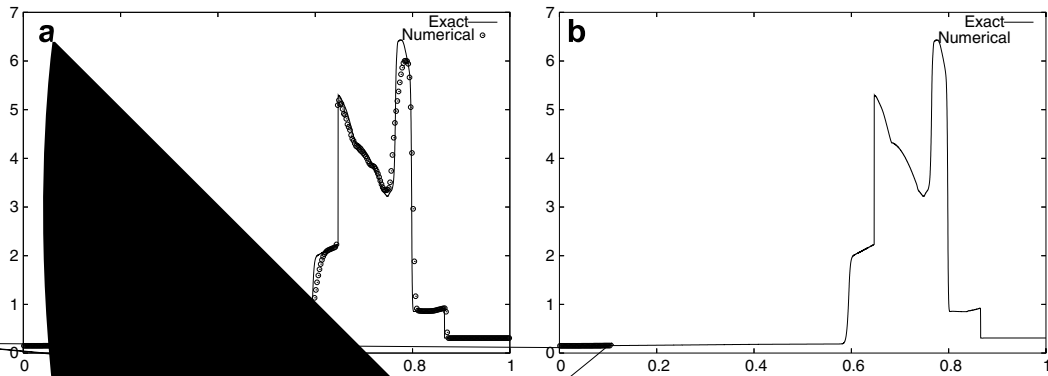


Fig. 19. Numerical solutions at  $t = 0.038$ . The 'exact' solutions are computed by the Roe-MUSCL finite volume method (a) and (b)  $CM^2$ -FVM-SL4.

Reflecting boundary conditions are used at both ends of computational domain. Two blast waves are generated by the explosion. The numerical solutions are computed by the Roe-MUSCL finite volume method and  $CM^2$ -FVM-SL4. The number of the mesh cells is 400. The characteristic velocity is 1. The numerical solutions are compared with the exact solutions. The numerical solutions are computed by the Roe-MUSCL finite volume method and  $CM^2$ -FVM-SL4. The numerical solutions are compared with the exact solutions. The numerical solutions are computed by the Roe-MUSCL finite volume method and  $CM^2$ -FVM-SL4.

The numerical solutions at  $t = 0.038$  with  $M_2 = 0$  are shown in Fig. 19. The numerical solutions are compared with the exact solutions. In this test,  $CM^2$ -FVM-SL4 is more accurate than Roe-MUSCL. We also find that there is no such difference in the numerical results for this case.

## 5. Discussions and conclusions

In this paper, we have introduced a new numerical method for solving the Euler conservation laws by using characteristic based approach. The numerical method is based on  $CM^2$ -FVM-SL4, the semi-Lagrangian update method for the multi-moment method. The PVs, which are referred to as the numerical solutions along the characteristic curves. The numerical solutions are compared with the exact solutions. The numerical solutions are computed by the Roe-MUSCL finite volume method and  $CM^2$ -FVM-SL4. The numerical solutions are compared with the exact solutions. The numerical solutions are computed by the Roe-MUSCL finite volume method and  $CM^2$ -FVM-SL4.

The presented method has been examined and compared with other high-order schemes, such as DG and (H)WENO schemes. The numerical method is competitive. The numerical formulation presented in this paper is suitable for multi-dimensional implementations on both structured and unstructured meshes and will be reported in a separate paper.

The CIP/multi-moment ( $CM^2$ ) concept provides a general basis for high-order schemes can be constructed. The moments used in this paper are straightforward and the integrated average of a physical field. Using at least two kinds of moments in the numerical formulation, a  $CM^2$  scheme is apparently different from the conventional methods of either finite difference or finite volume type, where only single moment is used. While is different from the DG formulation though multi-moments are also used in the DG method.  $CM^2$  formulation is more flexible and allows more existing numerical techniques being implemented in its framework. We have used a semi-Lagrangian approach to update the PVs in the present study, but by no means limit ourselves to this formulation. Eulerian time integration based on  $CM^2$ -FVM will be also reported soon.

## References

- [1] P. Colella, P. Woodward, The piecewise parabolic method for gas-dynamical simulations, *J. Comput. Phys.* 54 (1984) 174.
- [2] B. Cockburn, C.W. Shu, TVB Runge–Kutta local projection discontinuous Galerkin finite element method for conservation laws II: general framework, *Math. Comput.* 52 (1989) 411.
- [3] B. Cockburn, S.Y. Lin, C.W. Shu, TVB Runge–Kutta local projection discontinuous Galerkin finite element method for conservation laws III: one-dimensional systems, *J. Comput. Phys.* 84 (1989) 90.
- [4] B. Cockburn, S. Hou, C.W. Shu, TVB Runge–Kutta local projection discontinuous Galerkin finite element method for conservation laws IV: the multidimensional case, *Math. Comput.* 54 (1990) 545.
- [5] B. Cockburn, C.W. Shu, The Runge–Kutta discontinuous Galerkin method for conservation laws V: the multidimensional systems, *J. Comput. Phys.* 141 (1998) 199.
- [6] A. Harten, High resolution schemes for hyperbolic conservation laws, *J. Comput. Phys.* 49 (1983) 357.
- [7] A. Harten, B. Engquist, S. Osher, S. Chakravarthy, Uniformly high order essentially nonoscillatory schemes, III, *J. Comput. Phys.* 71 (1987) 231.
- [8] S. Li, M. Shimuta, F. Xiao, A 4th-order and single-cell-based advection scheme on unstructured grids using multi-moments, *Comput. Phys. Comm.* 173 (2005) 17.
- [9] G. Jiang, C.W. Shu, Efficient implementation of weighted ENO schemes, *J. Comput. Phys.* 126 (1996) 202.
- [10] P.D. Lax, Weak solutions of nonlinear hyperbolic equations and their numerical computation, *Commun. Pure Appl. Math.* 7 (1954) 159.
- [11] X.D. Liu, S. Osher, T. Chan, Weighted essentially non-oscillatory schemes, *J. Comput. Phys.* 115 (1994) 200.
- [12] J. Qiu, C.W. Shu, Hermite WENO schemes and their application as limiters for Runge–Kutta discontinuous Galerkin method: one-dimensional case, *J. Comput. Phys.* 193 (2003) 115.
- [13] P.L. Roe, Approximate Riemann solvers, parameter vectors, and difference schemes, *J. Comput. Phys.* 43 (1981) 357.
- [14] R. Sanders, A third-order accurate variation nonexpansive difference scheme for single nonlinear conservation laws, *Math. Comput.* 51 (1988) 535.
- [15] C.W. Shu, TVB uniformly high-order schemes for conservation laws, *Math. Comput.* 49 (1987) 105.
- [16] C.W. Shu, Total-variation-diminishing time discretizations, *SIAM J. Sci. Stat. Comput.* 9 (1988) 1073.
- [17] C.W. Shu, S. Osher, Efficient implementation of essentially non-oscillatory shock capturing schemes, *J. Comput. Phys.* 77 (1988) 439.
- [18] C.W. Shu, S. Osher, Efficient implementation of essentially non-oscillatory shock capturing schemes, II, *J. Comput. Phys.* 83 (1989) 32.
- [19] G. Sod, A survey of several finite difference methods for systems of non-linear conservation laws, *J. Comput. Phys.* 27 (1978) 1.
- [20] R. Tanaka, T. Nakamura, T. Yabe, Constructing exactly conservative scheme in a non-conservative form, *Comput. Phys. Commun.* 126 (2000) 232.
- [21] B. van Leer, Towards the ultimate conservative difference scheme. V. A second order sequel to Godunov’s method, *J. Comput. Phys.* 32 (1979) 101.
- [22] B. van Leer, Flux-vector splitting for the Euler equations, *Lecture Notes Phys.* 170 (1982) 507.
- [23] Z.J. Wang, Spectral (finite) volume method for conservation laws on unstructured grids: basic formulation, *J. Comput. Phys.* 178 (2002) 210.
- [24] Z.J. Wang, Y. Liu, Spectral (finite) volume method for conservation laws on unstructured grids II: extension to two-dimensional scalar equation, *J. Comput. Phys.* 179 (2002) 665.
- [25] Z.J. Wang, Y. Liu, Spectral (finite) volume method for conservation laws on unstructured grids III: one-dimensional systems and partition optimization, *J. Sci. Comput.* 20 (2004) 137.
- [26] Z.J. Wang, Y. Liu, L. Zhang, Spectral (finite) volume method for conservation laws on unstructured grids IV: extension to two-dimensional systems, *J. Comput. Phys.* 194 (2004) 716.
- [27] P. Woodward, P. Colella, The numerical simulation of two-dimensional fluid flow with strong shocks, *J. Comput. Phys.* 54 (1984) 115.
- [28] F. Xiao, T. Yabe, Completely conservative and oscillation-less semi-Lagrangian schemes for advection transportation, *J. Comput. Phys.* 170 (2001) 498.
- [29] F. Xiao, T. Yabe, X. Peng, H. Kobayashi, Conservative and oscillation-less atmospheric transport schemes based on rational functions, *J. Geophys. Res.* 107 (2002) 4609.
- [30] F. Xiao, Profile-modifiable conservative transport schemes and a simple multi integrated moment formulation for hydrodynamics, in: S. Armfield, P. Morgan, K. Srinivas (Eds.), *Computational Fluid Dynamics 2002*, Springer, 2003, p. 106.
- [31] F. Xiao, A. Ikebata, An efficient method for capturing free boundary in multi-fluid simulations, *Int. J. Numer. Method Fluid* 42 (2003) 187.
- [32] F. Xiao, Unified formulation for compressible and incompressible flows by using multi integrated moment method: one-dimensional inviscid compressible flow, *J. Comput. Phys.* 195 (2004) 629.
- [33] F. Xiao, R. Akoh, S. Li, Unified formulation for compressible and incompressible flows by using multi-integrated moments II: multi-dimensional version for compressible and incompressible flows, *J. Comput. Phys.* 213 (2006) 31.
- [34] F. Xiao, A. Ikebata, T. Hasegawa, Numerical simulations of free-interface fluids by a multi integrated moment method, *Comput. Struct.* 83 (2005) 409.
- [35] F. Xiao, X. Peng, A convexity preserving scheme for conservative advection transport, *J. Comput. Phys.* 198 (2004) 389.

- [36] T. Yabe, T. Aoki, A universal solver for hyperbolic-equations by cubic-polynomial interpolation. 1. One-dimensional solver, *Comput. Phys. Commun.* 66 (1991) 219.
- [37] T. Yabe, R. Tanaka, T. Nakamura, F. Xiao, Exactly conservative semi-Lagrangian scheme (CIP-CSL) in one dimension, *Mon. Weather Rev.* 129 (2001) 332.
- [38] T. Yabe, F. Xiao, T. Utsumi, The constrained interpolation profile method for multiphase analysis, *J. Comput. Phys.* 169 (2001) 556.